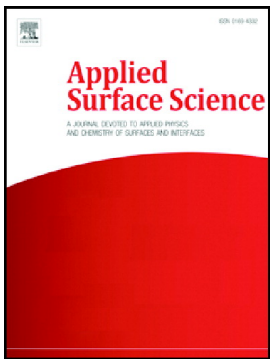

Facile fabrication of perovskite-incorporated hierarchically mesoporous/macroporous silica for efficient photoassisted-Fenton degradation of dye

Thi To Nga Phan, Aleksandar N. Nikoloski, Parisa Arabzadeh Bahri, Dan Li

PII: S0169-4332(19)31842-2
DOI: https://doi.org/10.1016/j.apsusc.2019.06.133
Reference: APSUSC 43090

To appear in: *Applied Surface Science*

Received date: 22 January 2019
Revised date: 28 May 2019
Accepted date: 12 June 2019

Please cite this article as: T.T.N. Phan, A.N. Nikoloski, P.A. Bahri, et al., Facile fabrication of perovskite-incorporated hierarchically mesoporous/macroporous silica for efficient photoassisted-Fenton degradation of dye, Applied Surface Science, https://doi.org/10.1016/j.apsusc.2019.06.133

Facile Fabrication of Perovskite-incorporated Hierarchically Mesoporous/Macroporous Silica for Efficient Photoassisted-Fenton Degradation of Dye

Thi To Nga Phan [1,2], Aleksandar N. Nikoloski [1], Parisa Arabzadeh Bahri [1], Dan Li [1]*

[1]Chemical and Metallurgical Engineering and Chemistry, School of Engineering and Information Technology, Murdoch University, Western Australia, Australia.

[2]Department of Organic and Petrochemical Technology, School of Chemical Engineering, Hanoi University of Science and Technology, Ha Noi, Viet Nam.

*Corresponding author. Telephone: +61 8 9360 2569; E-mail: l.li@murdoch.edu.au .

Abstract

$LaFeO_3$-doped hierarchically mesoporous/macroporous silica (LFO/MMS) was prepared for the first time by impregnation method and then calcination. The sample was characterized in detail, suggesting the successful incorporation of LFO into MMS which was consisting of mesopores and macropores. The high surface area, accessible pores as well as low band gap energy supported its high performance towards efficient photoassisted-Fenton degradation of dye under visible light irradiation. Rhodamine B (RhB), which has been widely used as one of typical synthetic dyes in textile industry, was selected as the dye model. It was found that the incorporation of LFO into the MMS support induced a significant enhancement in the visible-light photo-Fenton catalytic performance, as compared with pure LFO. The degradation rate using LFO/MMS under the conditions (temperature = 25 °C, catalyst dosage = 1 g L^{-1}, initial dye concentration = 10 mg L^{-1}, initial H_2O_2 concentration = 10 mM and

initial pH = 6) was 95.6% after 90-min exposure to the visible light. This was 7% and 19.8% greater than that of LFO and MMS, respectively. In particular, the pseudo-first-order reaction rate constant for LFO/MMS was 0.0367 min^{-1}, which was approximately 2 times higher than that for pure LFO (0.0215 min^{-1}). The newly developed catalyst, LFO/MMS, showed a good stability for recycle and reuse, which is crucial for its potential use in industrial application.

Keywords: $LaFeO_3$; mesoporous; macroporous; silica; photo-Fenton

1. Introduction

Recently, hierarchically structured porous materials have attracted increasing research interest due to their diversity and performance [1-3]. These materials well integrate multiple levels of pores from structure; and present multimodal pore size distributions from micropores (< 2 nm), mesopores (2 nm – 50 nm) to macropores (> 50 nm), which can be micro-meso, micro-macro, meso-macro, micro-meso-macro or meso-meso-macro [4]. For example, Liu *et al.* reported that MnO_2 hollow submicrospheres assembled by one-dimension nanorods building blocks with rich mesoporosity [5]. The resulting material showed superior catalytic performance and stability in the Fenton degradation of methylene blue (MB) [5]. Tao's group prepared the catalysts by loading Fe_2O_3 (the size of hundreds nanometres) into the hierarchically porous silica (HPS) skeleton, which exhibited the features of micropores, mesopores and macropores [6]. The BET surface areas, pore sizes and volumes were larger than those of commercial Fe_2O_3; which might greatly facilitate the molecular diffusion inside the catalysts and in turn improved the photo-Fenton degradation of azo-dye Orange II [6]. The hierarchically meso/macroporous TiO_2 showed improved reactivity and light harvesting capability, thanks to the macrochannels providing a light-transfer path for incident photon to penetrate inside the porous frameworks [7]. Hierarchically porous TiO_2 was also used as host matrix to incorporate or stabilize other components to form highly efficient photocatalysts for

dye degradation [8, 9]. As can be seen, the combination of high surface area arising from the microporous or/and mesoporous structure and accessible diffusion pathways given by the macroporous channels shows advantageous features; which have been found not only benefit for the use in water treatment, but also in other fields, e.g. chemical catalysis, gas storage, water purification and separation [10]. Especially in comparison to mono-sized porous material, hierarchically porous materials can always endow improved properties and thereby are of great interest [11].

In general, a template or the combination of two or more is required when building up these hierarchically porous complexes. For example, Wang and co-workers employed poly(methacrylic acid) as a spherical soft template to synthesize metastable β-Ag_2WO_4 using the precipitation reaction between $AgNO_3$ and Na_2WO_4 [12]. The obtained β-Ag_2WO_4 possessed a large specific surface area (165.5 m^2 g^{-1}) and hierarchically porous structure which was consisting of micropores, mesopores, and macropores. Its use removed approximately 90% of MO and phenol after 325-min and 180-min exposure to UV irradiation [12]. Lei *et al.* prepared hierarchically porous ZnO using urea and trisodium citrate as the templates in the hydrothermal reaction followed by calcination [13]. The obtained ZnO microspheres showed a significantly enhanced photocatalytic performance in the removal of methylene blue (MB) than commercial ZnO and TiO_2 [13]. In 10^{-5} M RhB solution, a complete removal by using the hierarchically porous ZnO was achieved after 80 min under UV irradiation; whilst that for commercial ZnO and TiO_2 was only ~30% and 60%, respectively [13].

In recent years, a great deal of effort has been contributed to developing different types of hierarchically porous hard templates, such as niobia [14], silica-alumina [15], and silica [14, 16-19], which can be used to achieve facile synthesis of catalysts with multimodal pores. Among them, silica has been found with a number of attractive features, such as moderate

hydrophobicity and non-charged framework [20]. However, so far, there has been no study exploring the use of hierarchically porous silica as a support to design a perovskite-integrated catalyst with a multimodal pore structure.

Lanthanum ferrite ($LaFeO_3$; LFO), which is one of ABO_3-type perovskite members, is an important functional material with a wide variety of potential applications in fuel cells [21, 22], chemical sensors [23, 24], and biosensors [25]. In addition, LFO has been well known as an efficient visible-light-driven catalyst due to its narrow band gap energy [26-28]. However, most of perovskite photocatalysts have low specific surface areas due to the agglomeration of particles during the synthesis, which limit their performances [29]. The literature suggests this issue be able to be solved if incorporating the perovskites into/onto the porous supports, which might improve the dispersion of catalyst particles on the support surface and restraint their agglomeration [30]. Peng *et al.* employed montmorillonite (MMT) as a support and developed $LaMO_3$/MMT (M = Fe, Co, Ni) photocatalysts for visible-light-initiated degradation of Rhodamine B (RhB) [31]. LFO/MMT exhibited remarkable adsorption capability and excellent performance with 99.34% of RhB removal after 90-min exposure to visible light [31]. Su and co-workers used SBA-16 as a support for depositing LFO and demonstrated the excellent photocatalytic performance of resulting composite for RhB degradation under visible light irradiation [29].

Taken account of the aforementioned benefits arising from the hierarchical pores of catalyst and the inherent properties of silica support, our research targeted at the development of novel LFO-incorporated hierarchically meso/macroporous silica for efficient visible-light-assisted Fenton catalytic degradation of dye. Rhodamine B was selected herein as a dye model, which is an important representative of xanthene dyes usually used in textile industry. It poses carcinogenic and teratogenic effects on the health of human beings and affects the growth of aquatic biota even when it presents at low concentration [32, 33]. Due to its

complex aromatic structure, RhB has good resistance to biodegradation and photolysis [34]. Photo-Fenton process is believed as a promising technique for RhB removal since several advantages, e.g. easy operation, high efficiency and cost effectiveness, can be seen over other treatment processes [35, 36]. Therefore, in this work, we synthesized LFO-doped meso/macroporous silica (LFO/MMS) by a facile method, impregnation and subsequent calcination. It exhibited improved photo-Fenton catalytic activity and good reusability in terms of RhB removal under visible light irradiation. The possible mechanisms governing the RhB degradation over LFO/MMS were also discussed in this paper. To the best of our knowledge, so far, there has been no open literature available on the design of LFO-doped meso/macroporous silica for use in the catalytic degradation of dye.

2. Experimental

2.1 Material Synthesis

Hierarchically meso/macroporous silica was prepared at 35 °C in a buffer solution (pH = 5.0) using P123 (Sigma-Aldrich) as a template based on the previous study [37, 38]. Typically, 1 g of P123 and 1.7 g of Na_2SO_4 (0.4 M) (Chem-Supply) were dissolved in 30 g of NaAc–HAc (Ac = acetate) (Rowe Scientific) buffer solution (pH = 5.0) (C_t = 0.04 M, where $C_t = C_{NaAc} + C_{HAc}$). The resulting solution was stirred to form a homogeneous solution, followed by the addition of 1.52 g of tetramethyl orthosilicate (TMOS; Sigma-Aldrich). The stirring was continued for 5 mins after adding TMOS. The solution was kept in an autoclave under a static condition for 24 h and was heated at 100 °C for another 24 h. After that, the autoclave was allowed to cool down to room temperature naturally. The obtained product was washed with deionised (DI) water and dried at 25 °C. It was then calcined in air at 550 °C for 5 h (ramp rate of 2 °C/min from 25 °C to 550 °C) to obtain the final meso/macroporous silica template (named as MMS).

$LaFeO_3$-doped meso/macroporous silica (LFO/MMS) was prepared by impregnation method and then calcination. Briefly, 4.33 g $La(NO_3)_3.6H_2O$ (Sigma-Aldrich), 4.04 g $Fe(NO_3)_3.9H_2O$ (Alta Aesar) and 4.608 g citric acid (Sigma-Aldrich) were dissolved in a mixture of 10 mL of DI water and 20 ml of ethanol to form a homogeneous solution. After stirring at room temperature for 3 h, 2 g of MMS was added to the above solution. The resulting solution was continuously stirred at 70 °C to evaporate the solvent, dried at 80 °C and then calcined at 700 °C for 4 h. The prepared catalyst was denoted as LFO/MMS. For comparison, LFO was prepared following the similar above procedures but in the absence of MMS.

2.2 Material Characterization

The powder samples were coated by sputtering of a thin platinum layer and examined by scanning electron microscopy (SEM, 5 kV, Zeiss 1555, VP-FESEM). X-ray powder diffraction (XRD) experiments were performed on a GBC eMMA X-ray diffractometer with Cu Kα radiation using an acceleration voltage of 35 kV and a current of 28 mA. The diffraction angle 2θ was scanned from 10 ° to 80 ° at a rate of 1 °/min. Nitrogen adsorption-desorption isotherms were measured at 77 K using SAPA2010 (Micromeritics Inc, USA). The surface area was determined from the linear part of the BET plot (P/P_0 = 0.05 ~ 0.30) and the pore size was calculated from the desorption branch of the isotherm by using Barrett-Joyner-Hallenda (BJH). The total pore volume was evaluated from the adsorbed nitrogen amount at a relative pressure of 0.98. Optical properties of the samples were characterized on a Perkin Elmer Lambda 750 UV/Vis/NIR spectrophotometer mounted with an integrating sphere accessor and using $BaSO_4$ as a reference.

2.3 Evaluation of Catalytic Activity Using RhB

Photocatalytic activity of the sample was conducted by adding 100 mg LFO, MMS or LFO/MMS into 100 mL of 10 mg L^{-1} RhB aqueous solution in a cylindrical Pyrex vessel

(300 mL), surrounding by a circulating water jacket to maintain solution temperature at ambient temperature. A photo-Fenton-like reaction was initiated by introducing 1 mL H_2O_2 to the suspension. A Xenon lamp (CEL-HX F300) was used with a 400 nm cut-off filter to provide visible light for photocatalytic degradation test. Before the photocatalytic reaction, the suspension was magnetically stirred in the dark for 30 mins to reach the adsorption-desorption equilibrium. Then, the suspension was exposed to visible light for 90 mins. Samples were taken from the suspension at selected time intervals and centrifuged at 10,000 rpm; the obtained supernatant was gathered for the UV-Vis absorption analysis using Perkin Elmer Lambda 750 UV/Vis spectrometer to determine the concentration of RhB solution. The photo-Fenton catalytic degradation % was calculated using formula given below:

$$Degradation\ (\%) = \left(1 - \frac{C_t}{C_0}\right) \times 100\% \quad (1)$$

where C_0 and C_t are the RhB concentrations before degradation and during degradation at a given period of time, respectively.

The total removal rate of dye using the as-prepared sample was calculated:

$$Removal\ rate\ (\%) = \left(1 - \frac{C_i}{C}\right) \times 100\% \quad (2)$$

where C and C_i are the concentration of RhB in the fresh solution before starting adsorption and the concentration of RhB at a given period of time during the adsorption – degradation process, respectively.

To understand the degradation kinetics of RhB as well as to quantitatively compare the catalytic performance of the materials under different reaction conditions, the zero, pseudo-first-order and pseudo-second-order kinetic models were used, as follows [39]:

Zero-order model: $\left(\frac{dC}{dt}\right) = -k_0$ (3)

Pseudo-first-order model: $\left(\frac{dC}{dt}\right) = -k_1 C$ (4)

Pseudo-second-order model: $\left(\frac{dC}{dt}\right) = -k_2C^2$ (5)

where C is the concentration of RhB; k_0, k_1, and k_2 are the apparent kinetic rate constants of zero-order, pseudo-first-order, and pseudo-second-order reaction, respectively; t is the reaction time.

The reusability of photocatalyst was performed by repeating the degradation tests (four times) under the similar above reaction conditions. The concentrations of Fe and La ions in the solution after the photo-Fenton degradation were determined *via* Inductively Coupled Plasma – Mass Spectrometry (ICP-MS, PerkinElmer's NexION 350) to monitor their leaching from LFO/MMS.

3. Results and Discussion

3.1 Material Characterization

Fig. 1 presents the XRD patterns of LFO/MMS, as compared with those of MMS and LFO. The characteristic peak detected at 2θ = 23^o in the XRD pattern of MMS indicates the presence of amorphous silica. It is noted that the intensity of this peak was significantly reduced when loading LFO into MMS. In the sample of LFO/MMS, all of the characteristic diffraction peaks well matched those observed in the XRD pattern of pure LFO, which was synthesized without the use of MMS support. It strongly suggests the successful loading of LFO, which exhibited the orthorhombic structure (JCPDS No. 37-1493), into MMS [40]. No apparent peaks representing impurities were found after the XRD analysis of LFO/MMS.

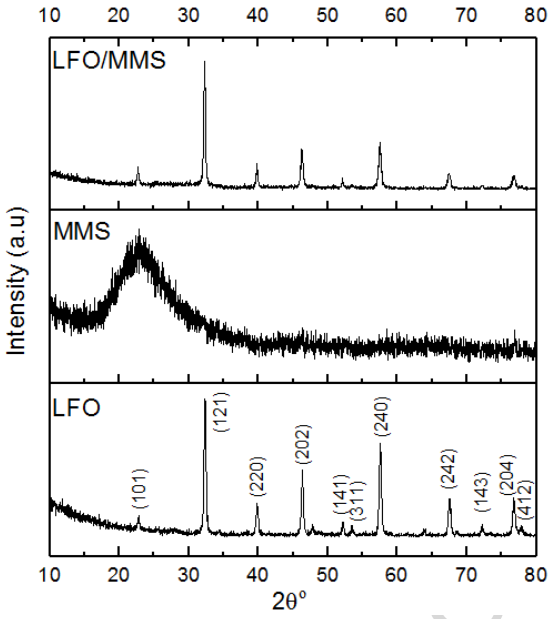

Fig. 1. XRD patterns of LFO, MMS, and LFO/MMS.

Fig. 2 shows the morphological property of LFO/MMS, as compared with MMS and LFO. The SEM image of LFO showed agglomeration of small particles with an average size of ~300 nm; whilst that of MMS exhibited a unique macroscopic network structure with macropores ranging 500 nm – 3 μm. The morphology of LFO/MMS observed by SEM was similar to that of MMS, implying that the structure of MMS support can be largely retained during the incorporation of LFO into MMS. In particular, the high-magnification SEM image revealed the presence of agglomerated particles inside the macropores of MMS, which were further examined by TEM as shown in Fig. 3. No significant LFO crystals or clumps were found separately from the particles of LFO/MMS during the SEM investigation.

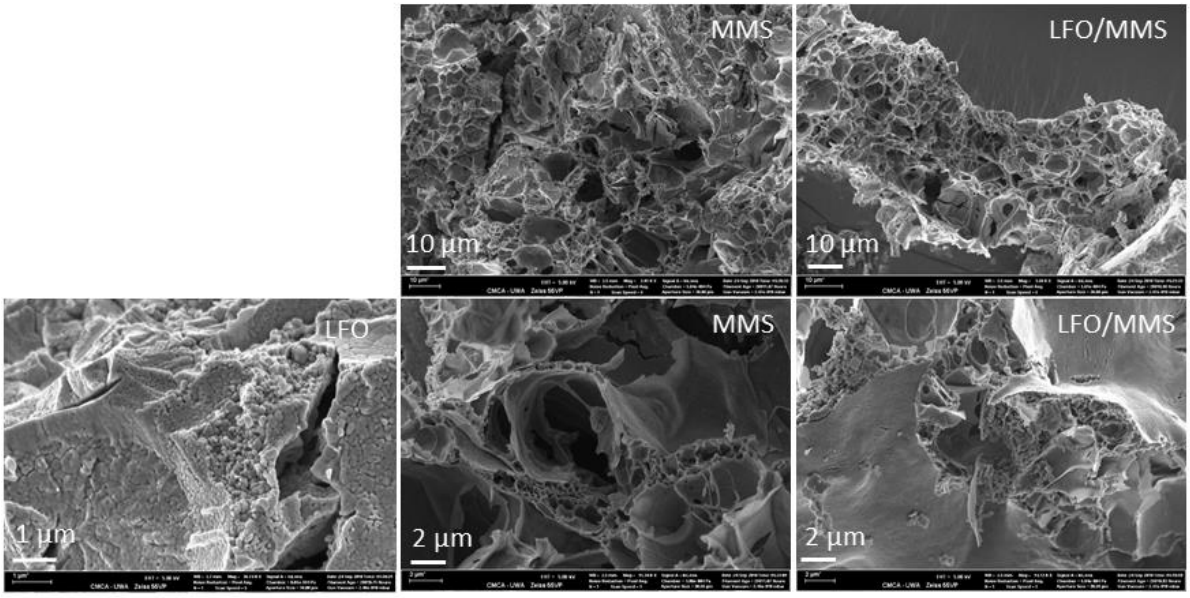

Fig. 2. SEM images of LFO, MMS and LFO/MMS.

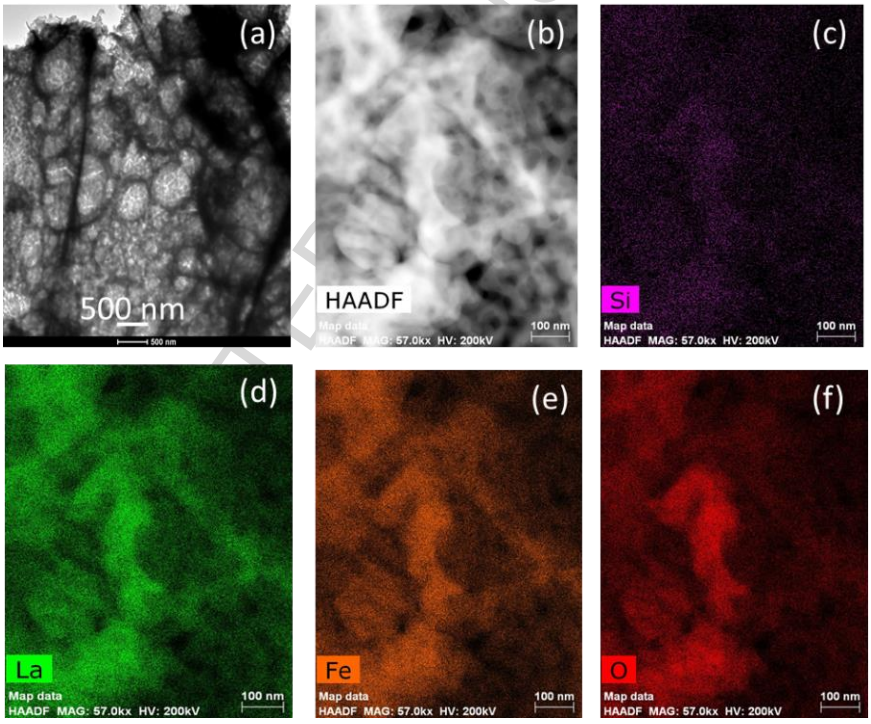

Fig. 3. (a) TEM image of LFO/MMS; (b) HAADF scanning TEM image of LFO/MMS and (c-f) the Si, La, Fe and O elemental mapping.

The TEM image (Fig. 3a) further confirmed the presence of macropores ranging from 500 nm – 3 µm in LFO/MMS, which is in a good agreement with the observation seen in Fig. 2.

The distribution of La and Fe, which were the elements of LFO, in the porous silica support MMS was shown in the elemental mapping images (Fig. 3c-f). This further confirmed the successful loading of LFO into MMS.

Fig. 4a shows the nitrogen adsorption-desorption isotherms of MMS and LFO/MMS both exhibited type IV accompanied by a type H2 hysteresis loop, suggesting the existence of typical mesoporous structure [41]. The BJH pore size distribution plots (Fig. 4b) further confirm MMS and LFO/MMS having mesoporous structures. It was reported that the decrease in the amount of physisorbed nitrogen was originated from a reduced specific surface [42]. This can be seen in the nitrogen adsorption-desorption isotherm of LFO/MMS (Fig. 4a), which may be attributed to the introduction of LFO into the porous structure of MMS, especially mesopores. The specific surface area and pore volume of LFO/MMS was 161.35 m^2/g and 0.28 cm^3/g, respectively, which was smaller than that of MMS 223.92 m^2/g and 0.56 cm^3/g. The average pore size of MMS and LFO/MMS calculated by the BJH method was approximately 8.28 nm and 6.20 nm, respectively. On the other side, the pure LFO powders showed the surface area of 8.06 m^2/g (Fig. 4a) and no apparent presence of mesopores (Fig. 4b). Therefore, as compared with LFO, LFO/MMS exhibited much greater specific surface area with accessible mesopores, providing more active sites and pathways for RhB removal.

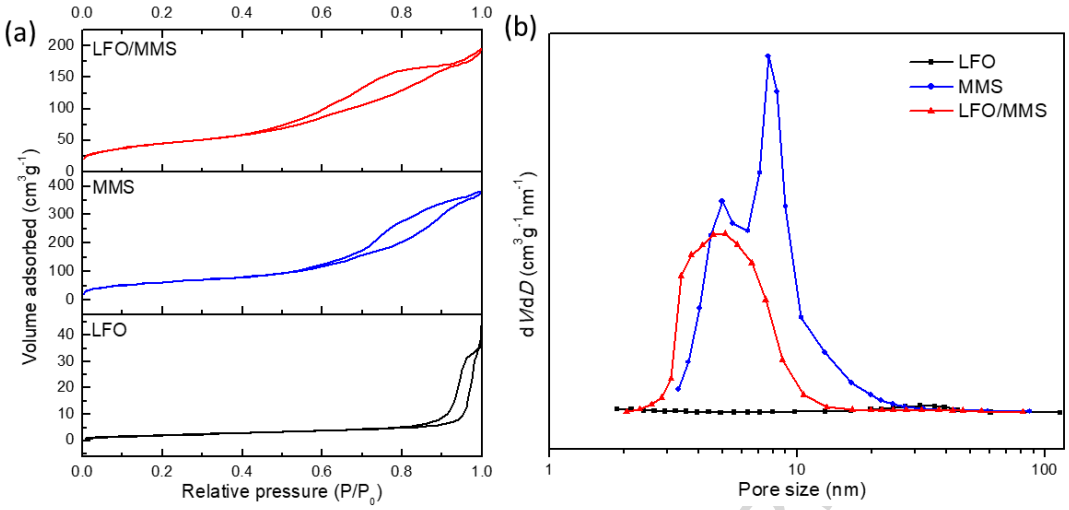

Fig. 4. (a) N_2 adsorption-desorption isotherms and (b) BJH pore size distributions of LFO, MMS and LFO/MMS.

Fig. S1 shows the FTIR spectra of LFO, MMS and LFO/MMS. In the FTIR spectrum of LFO, a peak at 535 cm^{-1} was seen, corresponding to the Fe-O stretching bands which are the characteristics of octahedral FeO_6 in LFO [43]. No other significant bonds appeared indicating relatively pure phase formation, which was further supported by the XRD patterns (Fig. 1). In the FTIR spectrum of MMS, the broad bands at 3472 cm^{-1} and 993 cm^{-1} are due to Si-OH stretching of surface silanol group and vibrational structure of Si–O–Si [44, 45]. When LFO was incorporated to MMS, a new band at around 528 cm^{-1} was observed in the spectrum of LFO/MMS. This new band could be attributed to the Fe-O stretching bands in LFO. This suggests that LFO was successfully incorporated in the MMS support. Moreover, the intensity of the band at 3472 cm^{-1} considerably decreased, which is probably due to the covering of silanol groups on the surface of MMS by LFO.

Fig. 5a shows the UV-vis absorption spectra of LFO and LFO/MMS compared to that of MMS, which exhibited no significant absorption in the range of visible light. LFO and LFO/MMS both exhibited a broad absorption peak in the visible region (400 nm – 800 nm). Their band gap energy could be estimated from the tangent lines in the plot of Kubelka-

Munck function $[F(R)h\upsilon]^2$ *versus* the energy of adsorbed light *hv* [46], as shown in Fig. 5b. The corresponding bandgap energy of LFO and LFO/MMS was 2.36 eV and 2.34 eV, respectively. The small bandgap of LFO/MMS may be ascribed to that the doping of perovskite into meso/macroporous MMS, which act as actives sites on the silica support to harvest visible light. Meanwhile, the observed macroporous channels (Fig. 2) play an important role as light-transfer paths, that allow photons reaching the active sties [47]. Indeed, in terms of visible-light-driven catalyst, a small band gap is the advantageous feature [48]. The small band gap energy of LFO/MMS reveals a feasibility of it absorbing visible light for efficient photo-Fenton catalytic degradation of dye.

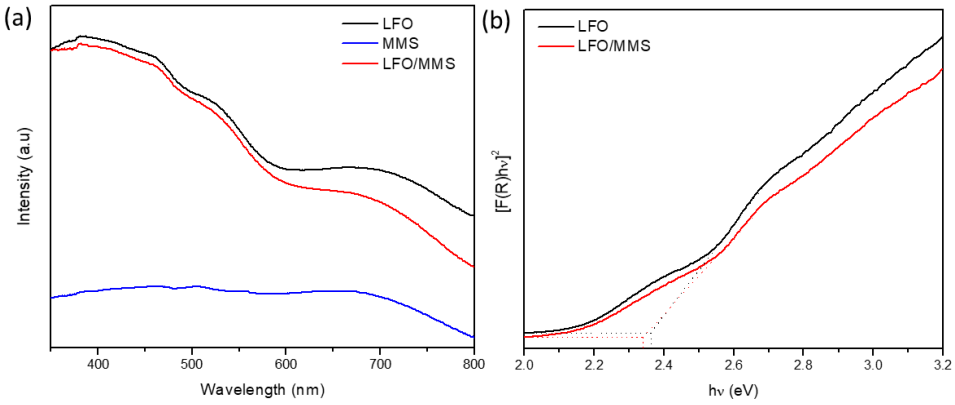

Fig. 5. (a) UV-vis absorption spectra of LFO, MMS and LFO/MMS and (b) corresponding bandgaps of LFO and LFO/MMS.

3.2 RhB Removal and Mechanisms

Fig. 6 shows the removal of RhB using LFO, MMS and LFO/MMS. Before initiating photo-Fenton reaction, MMS adsorbed ~50% of RhB from water as compared with negligible adsorption over LFO (~2%). This can be explained by the structural characteristics of MMS, e.g. greater specific area and porosity, which may offer extra spaces and pathways to enhance RhB adsorption. More importantly, MMS, which was made of silica and possessed ample amount of silanol groups on its surface, could bind to the carboxyl groups of RhB through

hydrogen bonds. The successful loading of LFO onto MMS might cover some of surficial silanol groups; this can be supported by the reduced intensity of the band at 3472 cm^{-1} in the FTIR spectrum of LFO/MMS when compared with that of MMS (Fig. S1). Only ~ 20% RhB was removed by LFO/MMS *via* adsorption in dark.

In Fig. 6, after photo-Fenton initiated by the use of visible light and introduction of H_2O_2, LFO/MMS exhibited the highest performance with 96.6% RhB being removed in 90 mins; whereas LFO and MMS could only remove 88.8% and 61.9% under the same reaction conditions. When using MMS, little RhB was removed by the photo-Fenton reaction. The extremely low degradation efficiency suggests that MMS could not work as the photo-Fenton catalyst under visible light, which is in a good agreement with the negligible light absorption property of MMS in the visible range (Fig. 5a). On the other side, LFO and LFO/MMS show much greater photo-Fenton activity for RhB removal. Especially, considering the same dosage of catalyst was adopted, the amount of LFO (theoretical 15 mol% LFO doping) in LFO/MMS participating the photo-Fenton reaction was much lower than that when using pure LFO. We also noted, during our experiment, the 90-min degradation of RhB using LFO/MMS and our visible light source in the absence of H_2O_2 was only ~4%.

It is commonly accepted that the interfacial Fe atoms (denoted as $\equiv Fe^{III}$) of perovskite-based catalysts can activate H_2O_2 to form hydroxyl radicals ($^{\bullet}OH$) during the Fenton-like reaction (Fig. 7) [49, 50]. Meanwhile, LFO/MMS catalyst can absorb the visible light to produce photogenerated electron-hole pairs following photocatalytic mechanism (Fig. 7) [51]. The electrons are trapped by H_2O_2 to generate highly reactive hydroxyl radicals ($^{\bullet}OH$) [49]. Possible mechanisms for the photo-Fenton-like reaction over LFO/MMS were proposed as illustrated in Fig. 7. Fig. S2 further verifies the important role of hydroxyl radicals in the photo-Fenton process by using ethanol as a scavenger of $^{\bullet}OH$ in the trapping experiment. When ethanol was added into the reaction solution, only ~ 40% RhB was degraded. It

confirms the presence of •OH in the reaction system as well as the essential role in the photo-Fenton-like degradation of RhB using LFO/MMS.

As compared with the relatively small surface area of LFO (8.06 m^2/g), the larger specific surface area of LFO/MMS (161.35 m^2/g), which benefited from the meso/macroporous support MMS, could enhance active sites exposed for photo-Fenton reaction and accessible channels for dye transport [52]. Moreover, the macropores may serve as mass-transfer paths and reduce transport resistance for dye molecules reaching active sites of LFO, which were located in the MMS [11]. Literature also supported that the introduction of macropores into mesopores frameworks could considerably improve the performance of mesoporous catalysts due to the enhanced diffusion of reactants and products [11].

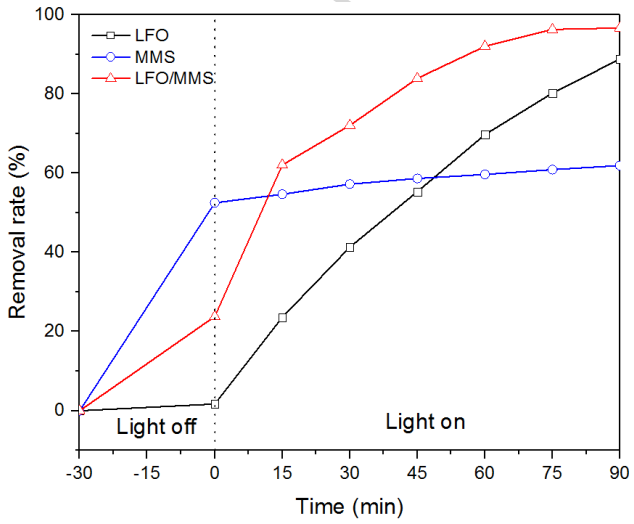

Fig. 6. Removal of RhB using LFO, MMS and LFO/MMS (reaction conditions: temperature = 25 °C, initial dye concentration = 10 mg L^{-1}, catalyst dosage = 1 g L^{-1}, initial H_2O_2 concentration = 10 mM and initial pH = 6).

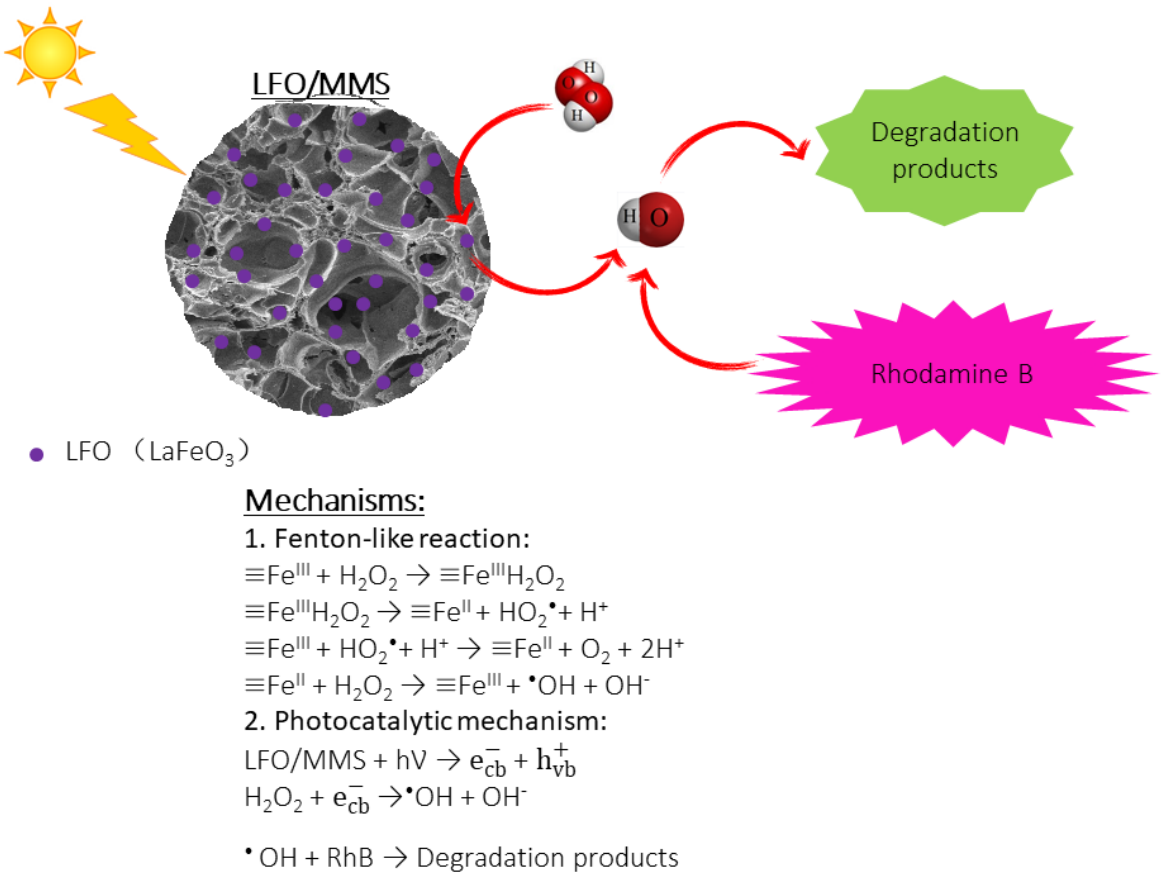

Fig. 7. Schematic of RhB degradation over LFO/MMS.

3.3 Photo-Fenton Removal of RhB using LFO/MMS

The effects of catalyst loading, dye concentration and solution pH on the degradation efficiency *versus* irradiation time were illustrated in Fig. 8a, b and c. In order to further study the RhB degradation kinetics of LFO/MMS under different conditions, the data were fitted by using the zero, first and second-order kinetic models [39]. The corresponding regression coefficients (R^2) and rate constants (k) were listed in Table 1. In general, the photo-Fenton catalytic degradation of RhB under different conditions conformed to the pseudo-first-order kinetic model, when compared with the zero-order or second-order kinetics.

Fig. 8a shows that the performance of the heterogeneous photo-Fenton reaction using LFO/MMS increased with an increase of catalyst dosage and then decreased after the loading was greater than 1 g L^{-1}. This can be explained by the higher turbidity of the reaction

suspension, induced by the increase of catalyst loading, which largely blocked the penetration of visible light and in turn reduced the formation of $^{\bullet}OH$ radicals. Ai *et al.* reported the similar observations for the degradation of Acid blue 29 by using iron-modified mesoporous silica in the photo-Fenton system [53]. Herein it was concluded that the catalyst dosage of 1g L^{-1} was the optimum amount with the highest pseudo-first-order reaction rate constant k_1 value of 0.0367 min^{-1}.

Table 1. Kinetic parameters for the degradation of RhB over LFO/MMS.

Variables	*Zero-order kinetic*		*First-order kinetic*		*Second-order kinetic*	
Catalyst dosage	k_0	R^2	k_1	R^2	k_2	R^2
0.5 g L^{-1}	0.0178	0.7242	0.0258	0.9796	0.0574	0.8654
0.8 g L^{-1}	0.0188	0.7269	0.0274	0.9965	0.0616	0.8647
1 g L^{-1}	0.0206	0.7440	0.0367	0.9948	0.1295	0.8994
1.2 g L^{-1}	0.0193	0.7301	0.0294	0.9941	0.0747	0.8498
H_2O_2 concentration	k_0	R^2	k_1	R^2	k_2	R^2
10 mM	0.0206	0.7440	0.0367	0.9948	0.1295	0.8994
15 mM	0.0215	0.7350	0.0409	0.9943	0.1713	0.9040
20 mM	0.0189	0.7196	0.0279	0.9804	0.0700	0.7629
25 mM	0.0180	0.7179	0.0253	0.9821	0.0561	0.7802
Initial pH	k_0	R^2	k_1	R^2	k_2	R^2
pH 4	0.0193	0.7387	0.0302	0.9963	0.0798	0.8642
pH 6	0.0215	0.7350	0.0409	0.9943	0.1713	0.9040
pH 8	0.0184	0.7301	0.0270	0.9903	0.0617	0.8755
pH 10	0.0166	0.6939	0.0209	0.9867	0.0358	0.8480

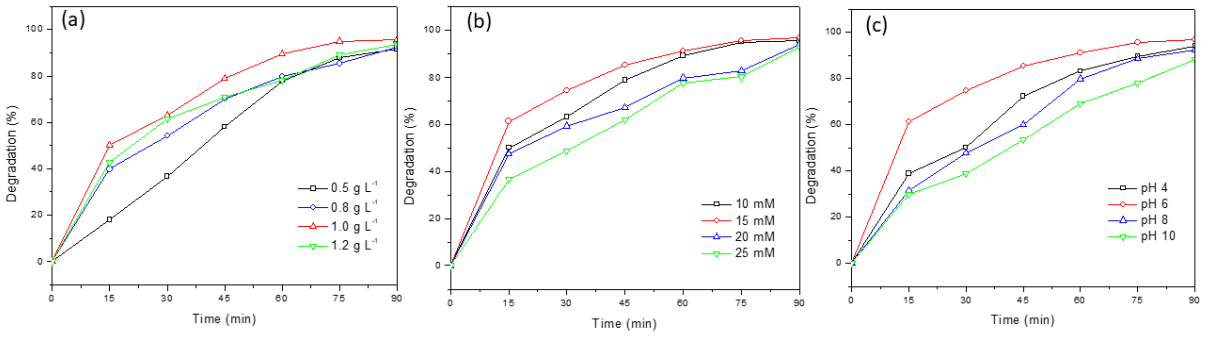

Fig. 8. Effect of catalyst dosage (initial H_2O_2 concentration = 10 mM) (a), H_2O_2 concentration (b) and pH (initial H_2O_2 concentration = 15 mM) (c) on photodegradation of RhB (reaction conditions (if no specified): temperature = 25 °C, catalyst dosage = 1 g L^{-1}, initial dye concentration = 10 mg L^{-1}, and initial pH = 6).

The influence of H_2O_2 concentration on the RhB removal was investigated by changing its concentration from 10 mM to 25 mM (Fig. 8b). In the photo-Fenton system, hydrogen peroxide plays an essential role to react with the catalyst and produce $^{\bullet}OH$ radicals, which attack organic dyes. When the H_2O_2 concentration was increased from 10 mM to 15 mM, the RhB removal was slightly enhanced due to the formation of more hydroxyl radicals. The highest RhB degradation rate, 96.9% (k_1 = 0.0409 min^{-1}), was observed at 15 mM H_2O_2. However, the continuous increase of H_2O_2 concentration from 20 mM to 25 mM lowered the RhB degradation. This could be ascribed to the reaction between the excess amount of H_2O_2 and $^{\bullet}OH$ radicals, producing less reactive hydroperoxyl radicals ($HO_2^{\bullet}$) (Eq. 6) [54]:

$$^{\bullet}OH + H_2O_2 \rightarrow HO_2^{\bullet} + H_2O \quad (6)$$

Fig. 8c shows the profiles of RhB degradation under different solution pHs (4 – 10); suggesting that the initial solution pH can significantly affect the degradation of RhB. The best activity was achieved at pH = 6 with 96.9% RhB removal (k_1 = 0.0409 min^{-1}). The reduced degradation rate when pH was lower than 6 (e.g. 94.2% at pH = 4) could be attributed to the fact that in acidic medium, overabundance of H^+ ions played a role as the scavengers of hydroxyl radicals (Eq. 7) [53]:

$$H^+ + {}^{\bullet}OH + e^- \rightarrow H_2O \quad (7)$$

On the other hand, when solution pH was at pH 8 or 10, the photo-Fenton catalytic activity of LFO/MMS was observed to decrease. This is due to the significant self-decomposition rate of hydrogen peroxide at high pH (Eq. 8) [55].

$$2H_2O_2 \rightarrow 2H_2O + O_2 \quad (8)$$

As discussed above, the optimal conditions for high-performace photo-Fenton degradation of RhB (96.9%) using LFO/MMS were suggested as: temperature = 25 °C, catalyst dosage = 1 g L^{-1}, initial dye concentration = 10 mg L^{-1}, initial H_2O_2 concentration = 15 mM and initial pH = 6. After finishing the first cycle of the photo-Fenton process, the LFO/MMS catalyst was collected by centrifugation, and then washed with DI water and dried in oven at 80 °C overnight. The recovered catalyst was applied for the next cycle of photo-Fenton catalytic degradation of RhB. At the fourth run, the photo-Fenton degradation of RhB after 90-min exposure to visible light irradiation reached 95%, as compared to 96.9 % at the first run. A slight drop (1.9%) of degradation rate (Fig. 9a), accompanied with almost unchanged crystal structure (Fig. 9b), implies the catalyst of LFO/MMS exhibited a good stability for recycle and reuse. The result of ICP-MS analysis also strongly supports this conclusion. It showed 4.823 mg L^{-1} La and 0.051 mg L^{-1} Fe in the solution after the photo-Fenton reaction, suggesting negligible amount of metal leaching from the catalyst and in turn good stability of LFO/MMS in reuse. Future work will use LFO/MMS to treat synthetic and actual dye-containing wastewater *via* photo-Fenton degradation to evaluate its potential, including its performance and reusability, for practical application.

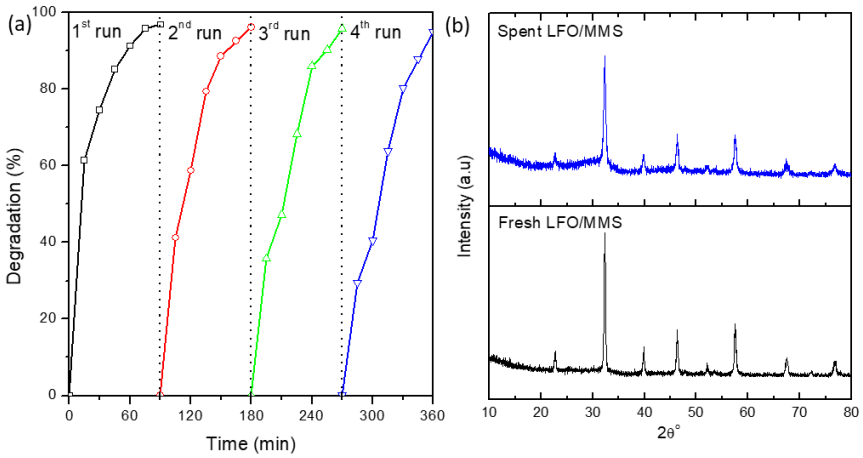

Fig. 9. (a) Stability of LFO/MMS over photo-Fenton-like catalytic degradation of RhB in four cycling runs (reaction conditions: temperature = 25 °C, catalyst dosage = 1 g L^{-1}, initial dye concentration = 10 mg L^{-1}, initial H_2O_2 concentration = 15 mM and initial pH = 6) and (b) XRD patterns of fresh LFO/MMS and spent LFO/MMS after 4 cycles of photo-Fenton-like catalytic degradation of RhB.

4. Conclusions

Novel $LaFeO_3$-doped meso/macroporous silica (LFO/MMS) catalyst was synthesized by the impregnation – calcination method. It efficiently removed RhB *via* the photoassisted-Fenton reaction and exhibited a good stability after 4 cycles of repetitive use. It has been found that the catalyst dosage, H_2O_2 concentration and initial pH solution had great influences on the degradation of RhB. 96.9% of RhB degradation rate was achieved in 10 mg L^{-1} RhB solution (pH of 6) when using 1 g L^{-1} LFO/MS and 15 mM H_2O_2 after 90-min visible light irradiation. The enhanced activity of LFO/MMS as compared with pure LFO was ascribed to its unique hierarchically meso/macroporous structure, which might greatly improve the transfer of visible light, exposure of active sites and diffusion of dye molecules.

Acknowledgement

T. Phan's PhD study is supported by Australia Awards Scholarship. This research was funded by Murdoch SEIT Small Grant Scheme (2016). The authors acknowledge the facilities, and the scientific and technical assistance of the Australian Microscopy & Microanalysis Research Facility at the Centre for Microscopy, Characterisation & Analysis, The University of Western Australia, a facility funded by the University, State and Commonwealth Governments.

References

[1] X. Tingting, X. Chunfeng, Z. Zhonglin, H. Xiaogang, Hierarchically Porous Carbon Materials Templated from Skeletonal Polyurethane Foam, Progress in Chemistry, 26 (2014) 1924-1929.
[2] D. Bradshaw, S. El-Hankari, L. Lupica-Spagnolo, Supramolecular templating of hierarchically porous metal–organic frameworks, Chemical Society Reviews, 43 (2014) 5431-5443.
[3] J. Du, X. Lai, N. Yang, J. Zhai, D. Kisailus, F. Su, D. Wang, L. Jiang, Hierarchically ordered macro−mesoporous TiO2− graphene composite films: improved mass transfer, reduced charge recombination, and their enhanced photocatalytic activities, ACS nano, 5 (2010) 590-596.
[4] M.-H. Sun, S.-Z. Huang, L.-H. Chen, Y. Li, X.-Y. Yang, Z.-Y. Yuan, B.-L. Su, Applications of hierarchically structured porous materials from energy storage and conversion, catalysis, photocatalysis, adsorption, separation, and sensing to biomedicine, Chemical Society Reviews, 45 (2016) 3479-3563.
[5] Y. Liu, Z. Chen, C.-H. Shek, C.M.L. Wu, J.K.L. Lai, Hierarchical Mesoporous MnO2 Superstructures Synthesized by Soft-Interface Method and Their Catalytic Performances, ACS Applied Materials & Interfaces, 6 (2014) 9776-9784.
[6] Z. Miao, S. Tao, Y. Wang, Y. Yu, C. Meng, Y. An, Hierarchically porous silica as an efficient catalyst carrier for high performance vis-light assisted Fenton degradation, Microporous and Mesoporous Materials, 176 (2013) 178-185.
[7] Y. Li, Z.Y. Fu, B.L. Su, Hierarchically structured porous materials for energy conversion and storage, Advanced Functional Materials, 22 (2012) 4634-4667.
[8] L. Pan, J.-J. Zou, S. Wang, Z.-F. Huang, X. Zhang, L. Wang, Enhancement of visible-light-induced photodegradation over hierarchical porous TiO2 by nonmetal doping and water-mediated dye sensitization, Applied Surface Science, 268 (2013) 252-258.
[9] G.-S. Shao, X.-J. Zhang, Z.-Y. Yuan, Preparation and photocatalytic activity of hierarchically mesoporous-macroporous TiO2− xNx, Applied Catalysis B: Environmental, 82 (2008) 208-218.
[10] J. Yu, L. Zhang, B. Cheng, Y. Su, Hydrothermal preparation and photocatalytic activity of hierarchically sponge-like macro-/mesoporous titania, The Journal of Physical Chemistry C, 111 (2007) 10582-10589.
[11] Z.-Y. Yuan, B.-L. Su, Insights into hierarchically meso–macroporous structured materials, Journal of Materials Chemistry, 16 (2006) 663-677.
[12] X. Wang, C. Fu, P. Wang, H. Yu, J. Yu, Hierarchically porous metastable β-Ag2WO4 hollow nanospheres: controlled synthesis and high photocatalytic activity, Nanotechnology, 24 (2013) 165602.
[13] A. Lei, B. Qu, W. Zhou, Y. Wang, Q. Zhang, B. Zou, Facile synthesis and enhanced photocatalytic activity of hierarchical porous ZnO microspheres, Materials Letters, 66 (2012) 72-75.
[14] P. Yang, T. Deng, D. Zhao, P. Feng, D. Pine, B.F. Chmelka, G.M. Whitesides, G.D. Stucky, Hierarchically ordered oxides, science, 282 (1998) 2244-2246.
[15] G. Gundiah, Macroporous silica-alumina composites with mesoporous walls, Bulletin of Materials Science, 24 (2001) 211-214.
[16] Z. Yang, K. Qi, J. Rong, L. Wang, Z. Liu, Y. Yang, Template synthesis of 3-D bimodal ordered porous silica, Chinese Science Bulletin, 46 (2001) 1785-1789.
[17] Q. Luo, L. Li, B. Yang, D. Zhao, Three-dimensional ordered macroporous structures with mesoporous silica walls, Chemistry Letters, 29 (2000) 378-379.
[18] D. Kuang, T. Brezesinski, B. Smarsly, Hierarchical porous silica materials with a trimodal pore system using surfactant templates, Journal of the American Chemical Society, 126 (2004) 10534-10535.

[19] W. Shi, S. Tao, Y. Yu, Y. Wang, W. Ma, High performance adsorbents based on hierarchically porous silica for purifying multicomponent wastewater, Journal of Materials Chemistry, 21 (2011) 15567-15574.
[20] N. Sasirekha, S.J.S. Basha, K. Shanthi, Photocatalytic performance of Ru doped anatase mounted on silica for reduction of carbon dioxide, Applied Catalysis B: Environmental, 62 (2006) 169-180.
[21] L. Liu, K. Sun, X. Li, M. Zhang, Y. Liu, N. Zhang, X. Zhou, A novel doped CeO2–LaFeO3 composite oxide as both anode and cathode for solid oxide fuel cells, international journal of hydrogen energy, 37 (2012) 12574-12579.
[22] M.-H. Hung, M.M. Rao, D.-S. Tsai, Microstructures and electrical properties of calcium substituted LaFeO3 as SOFC cathode, Materials chemistry and Physics, 101 (2007) 297-302.
[23] J. Qin, Z. Cui, X. Yang, S. Zhu, Z. Li, Y. Liang, Synthesis of three-dimensionally ordered macroporous LaFeO3 with enhanced methanol gas sensing properties, Sensors and Actuators B: Chemical, 209 (2015) 706-713.
[24] Z. Dai, C.-S. Lee, B.-Y. Kim, C.-H. Kwak, J.-W. Yoon, H.-M. Jeong, J.-H. Lee, Honeycomb-like periodic porous LaFeO3 thin film chemiresistors with enhanced gas-sensing performances, ACS applied materials & interfaces, 6 (2014) 16217-16226.
[25] G. Wang, J. Sun, W. Zhang, S. Jiao, B. Fang, Simultaneous determination of dopamine, uric acid and ascorbic acid with LaFeO 3 nanoparticles modified electrode, Microchimica Acta, 164 (2009) 357-362.
[26] S. Thirumalairajan, K. Girija, N.Y. Hebalkar, D. Mangalaraj, C. Viswanathan, N. Ponpandian, Shape evolution of perovskite LaFeO 3 nanostructures: a systematic investigation of growth mechanism, properties and morphology dependent photocatalytic activities, RSC Advances, 3 (2013) 7549-7561.
[27] R.D. Kumar, R. Thangappan, R. Jayavel, Synthesis and characterization of LaFeO3/TiO2 nanocomposites for visible light photocatalytic activity, Journal of Physics and Chemistry of Solids, 101 (2017) 25-33.
[28] P.S. Tang, M.B. Fu, H.F. Chen, F. Cao, Synthesis of nanocrystalline LaFeO3 by precipitation and its visible-light photocatalytic activity, in: Materials Science Forum, Trans Tech Publ, 2011, pp. 150-154.
[29] H. Su, L. Jing, K. Shi, C. Yao, H. Fu, Synthesis of large surface area LaFeO 3 nanoparticles by SBA-16 template method as high active visible photocatalysts, Journal of Nanoparticle Research, 12 (2010) 967-974.
[30] L. Li, Y. Song, B. Jiang, K. Wang, Q. Zhang, A novel oxygen carrier for chemical looping reforming: LaNiO3 perovskite supported on montmorillonite, Energy, 131 (2017) 58-66.
[31] K. Peng, L. Fu, H. Yang, J. Ouyang, Perovskite LaFeO 3/montmorillonite nanocomposites: synthesis, interface characteristics and enhanced photocatalytic activity, Scientific reports, 6 (2016) 19723.
[32] L. Hu, F. Yang, W. Lu, Y. Hao, H. Yuan, Heterogeneous activation of oxone with CoMg/SBA-15 for the degradation of dye Rhodamine B in aqueous solution, Applied Catalysis B: Environmental, 134-135 (2013) 7-18.
[33] E. Baldev, D. MubarakAli, A. Ilavarasi, D. Pandiaraj, K.A.S.S. Ishack, N. Thajuddin, Degradation of synthetic dye, Rhodamine B to environmentally non-toxic products using microalgae, Colloids and Surfaces B: Biointerfaces, 105 (2013) 207-214.
[34] W. Liu, Y. Yu, L. Cao, G. Su, X. Liu, L. Zhang, Y. Wang, Synthesis of monoclinic structured BiVO4 spindly microtubes in deep eutectic solvent and their application for dye degradation, Journal of Hazardous Materials, 181 (2010) 1102-1108.
[35] T.T.N. Phan, A.N. Nikoloski, P.A. Bahri, D. Li, Optimizing photocatalytic performance of hydrothermally synthesized LaFeO3 by tuning material properties and operating conditions, Journal of Environmental Chemical Engineering, 6 (2018) 1209-1218.

[36] T.T.N. Phan, A.N. Nikoloski, P.A. Bahri, D. Li, Heterogeneous photo-Fenton degradation of organics using highly efficient Cu-doped LaFeO3 under visible light, Journal of Industrial and Engineering Chemistry, 61 (2018) 53-64.
[37] H. Wang, X. Zhou, M. Yu, Y. Wang, L. Han, J. Zhang, P. Yuan, G. Auchterlonie, J. Zou, C. Yu, Supra-assembly of siliceous vesicles, Journal of the American Chemical Society, 128 (2006) 15992-15993.
[38] C. Zhao, J. Yang, Y. Wang, B. Jiang, Well-Dispersed Nanoscale Zero-Valent Iron Supported in Macroporous Silica Foams: Synthesis, Characterization, and Performance in Cr (VI) Removal, Journal of Materials, 2017 (2017).
[39] N.A. Youssef, S.A. Shaban, F.A. Ibrahim, A.S. Mahmoud, Degradation of methyl orange using Fenton catalytic reaction, Egyptian Journal of Petroleum, 25 (2016) 317-321.
[40] Y. Wang, J. Zhu, L. Zhang, X. Yang, L. Lu, X. Wang, Preparation and characterization of perovskite LaFeO3 nanocrystals, Materials Letters, 60 (2006) 1767-1770.
[41] K. Sing, The use of nitrogen adsorption for the characterisation of porous materials, Colloids and Surfaces A: Physicochemical and Engineering Aspects, 187-188 (2001) 3-9.
[42] M. Fröba, R. Köhn, G. Bouffaud, O. Richard, G. van Tendeloo, Fe2O3 nanoparticles within mesoporous MCM-48 silica: in situ formation and characterization, Chemistry of materials, 11 (1999) 2858-2865.
[43] P.V. Gosavi, R.B. Biniwale, Pure phase LaFeO3 perovskite with improved surface area synthesized using different routes and its characterization, Materials Chemistry and Physics, 119 (2010) 324-329.
[44] H.-J. Jeon, S.-C. Yi, S.-G. Oh, Preparation and antibacterial effects of Ag–SiO2 thin films by sol–gel method, Biomaterials, 24 (2003) 4921-4928.
[45] D. Uhlmann, S. Liu, B.P. Ladewig, J.C. Diniz da Costa, Cobalt-doped silica membranes for gas separation, Journal of Membrane Science, 326 (2009) 316-321.
[46] E. García-López, G. Marcì, F. Puleo, V. La Parola, L.F. Liotta, La1−xSrxCo1−yFeyO3−δ perovskites: Preparation, characterization and solar photocatalytic activity, Appl. Catal., B., 178 (2015) 218-225.
[47] X. Wang, J.C. Yu, C. Ho, Y. Hou, X. Fu, Photocatalytic activity of a hierarchically macro/mesoporous titania, Langmuir, 21 (2005) 2552-2559.
[48] D. Wang, T. Kako, J. Ye, Efficient photocatalytic decomposition of acetaldehyde over a solid-solution perovskite (Ag0. 75Sr0. 25)(Nb0. 75Ti0. 25) O3 under visible-light irradiation, Journal of the American Chemical Society, 130 (2008) 2724-2725.
[49] L. Li, X. Wang, Y. Lan, W. Gu, S. Zhang, Synthesis, photocatalytic and electrocatalytic activities of wormlike GdFeO3 nanoparticles by a glycol-assisted sol–gel process, Industrial & Engineering Chemistry Research, 52 (2013) 9130-9136.
[50] L. Ju, Z. Chen, L. Fang, W. Dong, F. Zheng, M. Shen, Sol‐Gel Synthesis and Photo‐Fenton‐Like Catalytic Activity of EuFeO3 Nanoparticles, Journal of the American Ceramic Society, 94 (2011) 3418-3424.
[51] J. Yang, R. Hu, W. Meng, Y. Du, A novel p-LaFeO 3/n-Ag 3 PO 4 heterojunction photocatalyst for phenol degradation under visible light irradiation, Chemical Communications, 52 (2016) 2620-2623.
[52] X. Yu, J. Yu, B. Cheng, M. Jaroniec, Synthesis of hierarchical flower-like AlOOH and TiO2/AlOOH superstructures and their enhanced photocatalytic properties, The Journal of Physical Chemistry C, 113 (2009) 17527-17535.
[53] A.N. Soon, B. Hameed, Degradation of Acid Blue 29 in visible light radiation using iron modified mesoporous silica as heterogeneous Photo-Fenton catalyst, Applied Catalysis A: General, 450 (2013) 96-105.
[54] F.F. Dias, A.A. Oliveira, A.P. Arcanjo, F.C. Moura, J.G. Pacheco, Residue-based iron catalyst for the degradation of textile dye via heterogeneous photo-Fenton, Applied Catalysis B: Environmental, 186 (2016) 136-142.
[55] M. Kasiri, H. Aleboyeh, A. Aleboyeh, Degradation of Acid Blue 74 using Fe-ZSM5 zeolite as a heterogeneous photo-Fenton catalyst, Applied Catalysis B: Environmental, 84 (2008) 9-15.

Highlights

- $LaFeO_3$-doped mesoporous/macroporous silica was studied for photo-Fenton
- Its structure and bandgap supported efficient photo-Fenton degradation of dye
- It was much more effective in removing dye compared to pure $LaFeO_3$
- Its use was optimized by varying solution pH, H_2O_2 and catalyst concentration
- It showed good stability and reusability